High-Density and Low-Crosstalk Multilayer Silicon Nitride Waveguide Superlattices With Air Gaps

Wen-ling Li, Jing-wei Liu, Guo-an Cheng, Rui-ting Zheng, and Xiao-ling Wu

***Abstract*—High-density and low-crosstalk waveguide arrays are critical components in optical phased arrays (OPAs) and are widely used in solid-state light detection and ranging (LiDAR). In this work, silicon nitride waveguide superlattices with air gaps are proposed and analyzed theoretically. Mode analysis shows that the introduced air gaps beside the waveguide help shorten the skin depth of the evanescent field and increase the effective index range of the waveguide under single mode conditions. Lower crosstalk is demonstrated between a pair of waveguides with air gaps compared with those without air gaps. On this basis, a waveguide superlattice with air gaps is designed by combining the eigenmode expansion method and particle swarm optimization. The crosstalk of the waveguide superlattice is optimized to −24.3 dB when the waveguide pitch is 0.9 μm, the propagation length is 1 mm, and the wavelength is 905 nm. The crosstalk is still below −22.4 dB under the typical process variations and over the wavelength range of 890 nm–920 nm. Therefore, the proposed air-gap waveguide superlattices with high density and low crosstalk offer opportunities to improve the beam steering performance of OPA chips in the near-infrared (NIR) waveband.**

***Index Terms*—Air gaps, optical crosstalk, waveguide arrays.**

I. Introduction

In recent years, chip-scale solid-state light detection and ranging (LiDAR) technology has attracted much attention in automotive and VR/AR applications due to its compact size, high reliability, and low cost. Optical phase arrays (OPAs) based on silicon photonics [1], [2], [3], [4], [5], [6], [7], [8], [9], [10], [11], [12], [13], [14], [15], [16], [17], [18], [19] have become a promising solid-state beam steering technology compared to microelectromechanical systems (MEMSs) and mechanical rotation methods due to their wide steering angle and flexible range of interest (ROI) selection.

For OPAs, the aliasing-free beam steering angle is negatively related to the spacing of the antenna array, which can reach 180 degrees at a half-wavelength spacing. However, as the spacing decreases, the crosstalk, i.e., power coupling, between the adjacent antennas (waveguide or grating) increases, leading to far-field sidelobes and beam quality degradation. Thus, suppressing the crosstalk in the antenna array becomes a key issue. According to coupled mode theory [20], the crosstalk between waveguides decreases as the mode overlap decreases or the effective index difference increases. To reduce the mode overlap, methods such as increasing the waveguide pitch, shortening the mode field skin depth, or adding an isolation structure can be used. Sparse and unevenly spaced arrays with large spacing between the antennas are proposed to achieve lower crosstalk [1], [6]: the uneven distribution breaks the constructive interference of the grating lobes so that the main lobe still has a large steering range. However, this also reduces the power of the main lobe and introduces intense background noise. In addition, methods such as increasing the thickness or width of the waveguides [21] are used to shorten the mode field skin depth. Furthermore, introducing photonic crystals [2], [22] or metamaterials between adjacent waveguides [23], [24], [25] can also decrease the overlap by isolation. To suppress crosstalk by increasing the effective index difference between waveguides, waveguide superlattices [8], [17], [26], [27], [28], bending waveguide arrays [9], [29], [30], [31] and waveguide arrays with asymmetrically located stripes [32] have been proposed.

Until now, most of the studies on OPA chips have focused on frequency modulation continuous wave (FMCW) LiDAR at a wavelength of 1,550 nm [1], [2], [3], [4], [5], [6], [7], [8], [9], [10], [11], [12], [13], [14], [15], [16], [17], based on silicon or silicon and silicon nitride hybrid waveguide reuse components in optical communication. Compared to the InGaAs or Ge photodetector for 1,550 nm application, the Si photodetector available in the wavelength range below 1,000 nm is more cost-effective. And Si single-photon detectors with high sensitivity have been developing rapidly in recent years and have been widely used in mechanical, MEMS, or flash LiDAR. Therefore, the LiDAR combined with Si photodetector and solid beam steering OPA chip will be a low-cost and attractive solution [18], [19]. Silicon nitride is one of the waveguide materials suitable for the 905 nm waveband OPA chips owing to its wide transparent window and low propagation loss [33]. For silicon waveguide arrays at a wavelength of 1,550 nm, crosstalk below −20 dB has been achieved by using a waveguide superlattice [26] or sinusoidal bending waveguide array [31] at half-wavelength spacing. However, for the silicon nitride waveguide arrays, the crosstalk is higher with the same spacing for the lower core-to-cladding refractive index ratio. Waveguide superlattices based on silicon

Manuscript received 5 November 2022; revised 13 December 2022; accepted 22 December 2022. Date of publication 26 December 2022; date of current version 4 January 2023. *(Corresponding author: Wen-ling Li.)*

Wen-ling Li is with the School of Nuclear Science and Technology, Beijing Normal University, Haining 314400, China, and also with the China Science Photon Chip (Haining) Technology Co., Ltd., Haining 314400, China (e-mail: wenlingli@mail.bnu.edu.cn).

Jing-wei Liu is with the China Science Photon Chip (Haining) Technology Co., Ltd., Haining 314400, China (e-mail: liujingwei@cspctech.com).

Guo-an Cheng, Rui-ting Zheng, and Xiao-ling Wu are with the School of Nuclear Science and Technology, Beijing Normal University, Beijing 100875, China (e-mail: gacheng@bnu.edu.cn; rtzheng@bnu.edu.cn; wuxl@bnu.edu.cn).

Digital Object Identifier 10.1109/JPHOT.2022.3232094

TABLE I
STRUCTURAL PARAMETERS OF AGW AND NAGW

Waveguide type	t_1	g_1	t_2	α	h_{top}	h_{bottom}	t_s	h_{ag}	β
AGW	75 nm	100 nm	275 nm	86°	$2.55\mu m$	$3\mu m$	$w_{ag}/2$	$450nm$	86°
NAGW	75 nm	100 nm	275 nm	86°	$2.55\mu m$	$3\mu m$	-	-	-

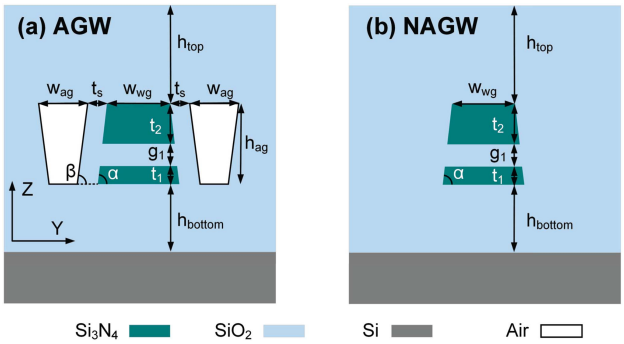

Fig. 1. The structures of AGW (a) and NAGW (b).

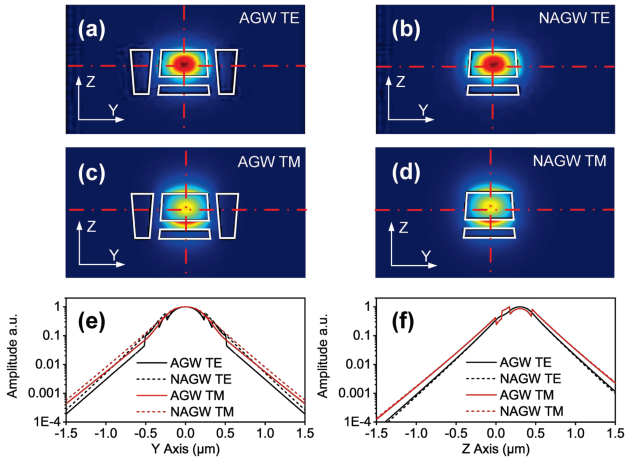

Fig. 2. Mode field of AGW and NAGW. (a) TE00 mode field of AGW; (b) TE00 mode field of NAGW; (c) TM00 mode field of AGW; (d) TM00 mode field of NAGW; (e) TE00 and TM00 field amplitude of AGW and NAGW along Y axis at Z = 0.25 μm; (d) TE00 and TM00 field amplitude of AGW and NAGW along Z axis at Y = 0 μm.

nitride are proven to suppress the crosstalk to -18 dB at the pitch of 1.5 μm in the communication waveband [34], still far beyond the half wavelength, indicating that more effort should be devoted to reducing the spacing. Notably, it is possible to increase the core-to-cladding refractive index ratio by using low-index cladding materials such as air since air gaps are demonstrated to be feasible in manufacturing integrated circuits (ICs) between metal lines to reduce capacitance [35]. However, as we know, no such work has been reported.

In this work, we propose an air-gap multilayer silicon nitride waveguide and theoretically analyze the mode field profile and the effective index of the waveguide. On this basis, multilayer silicon nitride waveguide superlattices with air gaps are designed and optimized to achieve low crosstalk. Calculations show that the crosstalk of the waveguide array is optimized to -24.3 dB at a waveguide pitch of 0.9 μm, a propagation length of 1 mm, and a wavelength of 905 nm. The crosstalk remains below -20 dB under the typical process variations and over the wavelength range of 890 nm–920 nm.

II. DESIGN AND OPTIMIZATION

A. The Structure and Mode Analysis of AGW and NAGW

The structures of the air-gap waveguide (AGW) and no air-gap waveguide (NAGW) are shown in Fig. 1. The NAGW is based on the asymmetric dual stripe (ADS) TriPleX waveguide [33], the waveguide core of which is composed of two silicon nitride layers and one silicon oxide layer sandwiched in between, and the cladding and substrate materials are silicon oxide and silicon, respectively, as shown in Fig. 1(b). The AGW is configured by introducing two air gaps beside a NAGW, as shown in Fig. 1(a).

The structural parameters of the AGW and NAGW are shown in Table I, where the height of the air gap h_{ag} is assumed to be the same as the core thickness, the top width of the air gap w_{ag} changes within the range of 125 nm–375 nm, and the thickness of the silicon oxide deposited on sidewall t_s is half of the air gap width w_{ag}, i.e., $t_s = w_{ag}/2$. The sidewall angle of the TriPleX waveguide α is typically within the range of $82°$ to $87°$, according to process experience [33]. Thus, α is assumed to be $86°$, and the sidewall angle of air-gap β is taken as the same value.

The mode field profiles of the NAGW and AGW are shown in Fig. 2. Here, the wavelength is 905 nm, the waveguide widths of NAGW and AGW are both $w_{wg} = 0.45$ μm, and other structural parameters are shown in Table I. The finite-difference eigenmode (FDE) solver of Ansys Lumerical software is used in this simulation.

Comparing the mode field distribution in the y direciton (Fig. 2(e)), it can be determined that the skin depth of the evanescent field of the AGW is shorter than that of the NAGW. And for both AGW and NAGW, TE00 mode has a shorter skin depth than the TM00 mode. The mode field distribution in the z direction is nearly the same for AGW and NAGW (Fig. 2(f)).

The reason for this is that the AGW has a higher core-cladding refractive index ratio only in the y direction since the refractive indices of silicon nitride, silicon oxide, and air at a wavelength of 905 nm are $n_{Si_3N_4} = 1.9965$, $n_{SiO_2} = 1.4503$, and $n_{air} = 1$, respectively.

The effective indices of NAGW and AGW are shown in Fig. 3, where the air-gap width $W_{ag} = 0$ nm corresponds to NAGW, and $W_{ag} = 125$ nm or 375 nm correspond to AGW. The waveguide width is in the range of 250 nm to 800 nm, and other structural parameters are listed in Table I. The maximum waveguide width of the single transverse electric (TE) mode is 0.59 μm for AGW, which exceeds the value of 0.50 μm for NAGW. And the maximum waveguide width of the single transverse magnetic (TM) mode is 0.63 μm for AGW, which is also larger than the

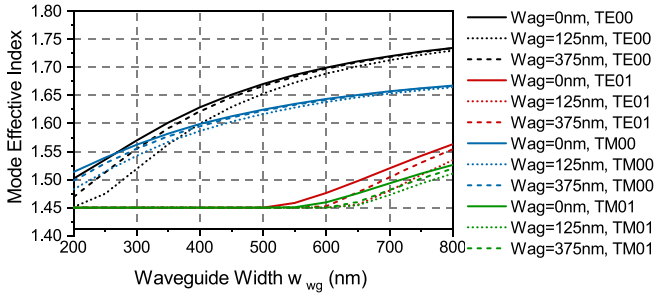

Fig. 3. The mode effective index changes with core width w_{wg} and air-gap width w_{ag} at a wavelength of 905 nm. The solid dotted and dashed lines correspond to air-gap widths of 0 nm, 125 nm, and 375 nm, respectively.

value of 0.54 μm for NAGW. The maximum effective index of the single-mode AGW is larger than that of the NAGW for both TE and TM mode, so it is easier for the AGW to introduce the effective index difference. And for both AGW and NAGW, the TE mode has a larger effective index range than the TM mode. Therefore, TE mode AGW is chosen in the following design due to the shortest skin depth and the largest effective index range.

B. Crosstalk of AGWs and NAGWs

According to the well-known coupled mode theory [20], the power coupling ratio from one waveguide to a neighbor waveguide, i.e., the crosstalk, is as follows:

$$\frac{\Delta P}{P_{in}} = F sin^2\left(\frac{\pi L}{2L_C}\right) \tag{1}$$

Here, P_{in} and ΔP are the input power and the coupling power, respectively, $F = 1/\{1 + [\Delta\beta/(2\kappa)]^2\}$ is the maximum coupling ratio, L is the propagation length, $L_C = \pi\sqrt{F}/(2\kappa)$ is the crossover length, and $\Delta\beta$ and κ are the propagation constant difference and the coupling strength between the two waveguides, respectively. The coupling strength κ is positively related to the overlap between the mode fields of the two waveguides.

For symmetric waveguides with $\Delta\beta = 0$, the maximum coupling ratio F is 1, and the crossover length L_C is $\pi/(2\kappa)$. For asymmetric waveguides, the maximum coupling ratio F depends on the ratio of $\Delta\beta/\kappa$. When the propagation constant difference $\Delta\beta$ is larger or the coupling strength κ is smaller, the maximum crosstalk is lower, and the crossover length L_C is shorter.

The crosstalk of symmetric and asymmetric AGWs and NAGWs is shown in Fig. 4(a)–(b). The widths of the symmetric waveguides are $w_1 = w$ and $2 = 0.45$ μm, and the widths of asymmetric waveguides are $w_1 = 0.45$ μm and $w_2 = 0.40$ μm.

For both cases, the pitch is 0.9 μm, the gap ratio, defined as the ratio of the air gap width to the inner side distance of adjacent waveguides, i.e., $w_{ag}/(pitch - w_1/2 - w_2/2)$, is 50%, and the other structural parameters are listed in Table I. The eigenmode expansion (EME) solver of Ansys Lumerical software is used in the simulation. As the propagation length increases, the crosstalk oscillates according to a sine function, as shown in Fig. 4(c) and (d). For symmetric waveguides, the crossover lengths of the NAGWs and AGWs are 52 μm and 95.5 μm, respectively,

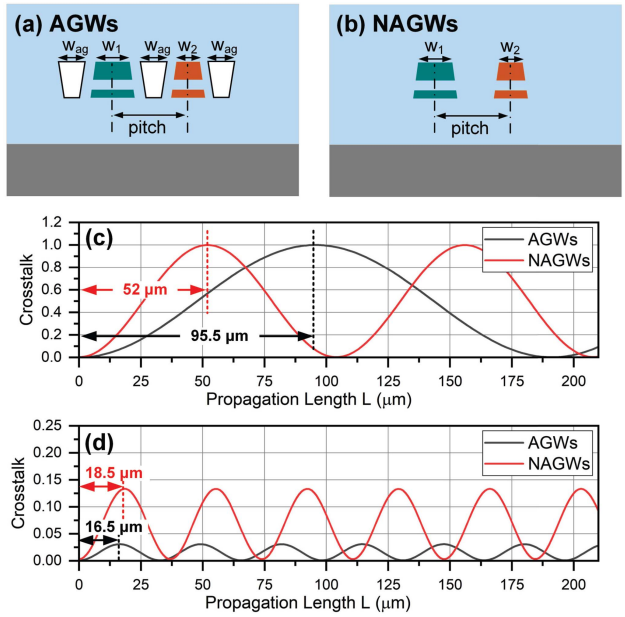

Fig. 4. Structure and crosstalk of a pair of AGWs and NAGWs at a wavelength of 905 nm. (a) and (b) are the structures of AGWs and NAGWs; (c) is the crosstalk of symmetric AGWs and NAGWs varying with propagation length, where the waveguide widths are $w_1 = w_2 = 0.45$ μm; (d) is the crosstalk of asymmetric AGWs and NAGWs varying with propagation length, where the waveguide widths are $w_1 = 0.45$ μm and $w_2 = 0.40$ μm; for both (c) and (d), the pitch is 0.9 μm, the gap ratio is 50%, and the other parameters are as listed in Table I.

at a wavelength of 905 nm. The AGW has a shorter crossover length, suggesting that the AGW has a lower coupling strength due to its shorter skin depth and smaller mode field overlap. For asymmetric NAGWs and AGWs, the respective maximum power coupling values are 0.131 and 0.031, and the crossover lengths are 18.5 μm and 16.5 μm at a wavelength of 905 nm. The crossover length of asymmetric waveguides is significantly smaller than that of symmetric waveguides. If the propagation length is in the range of 100 μm to 1 mm, which is typical for the waveguide array of an OPA, the crossover length is much shorter than the propagation length, and the maximum crosstalk is independent of the propagation length, mainly depending on the maximum coupling ratio.

The maximum crosstalk values versus waveguide widths for asymmetric AGWs and NAGWs are shown in Fig. 5. Here, the waveguide pitch is still 0.9 μm, the waveguide width is in the range of 0.25 μm to 0.60 μm, the gap ratio is 50%, the propagation length is $L = 1$ mm, and the other structure parameters are as listed in Table I. The minimum values of the maximum crosstalk for single-mode AGWs and NAGWs are -24.5 dB and -18.4 dB at 905 nm, respectively. The crosstalk of AGWs is lower than that of NAGWs due to smaller skin depths and larger propagation constant differences due to the wider effective index range.

C. Design of AGW Superlattices

In the waveguide array, power coupling appears between any two waveguides, leading to difficulty in suppressing the

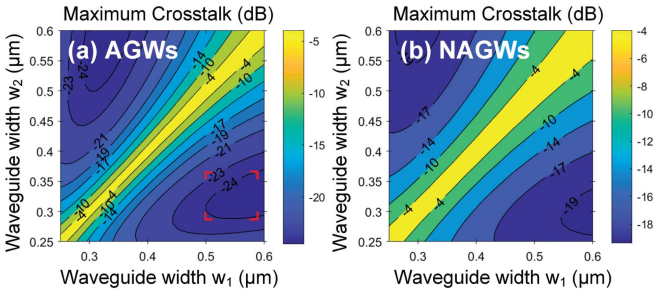

Fig. 5. Maximum crosstalk of a pair of asymmetric AGWs (a) and NAGWs (b) at a wavelength of 905 nm. The pitch is 0.9 μm, the propagation length is 1 mm, the gap ratio is 50%, and the other structural parameters are listed in Table. The maximum widths of the single-mode AGW and NAGW are 0.59 μm and 0.50 μm, respectively. The red box in (a) marks the waveguide width range covering the crosstalk range below -24 dB and satisfying the single mode condition.

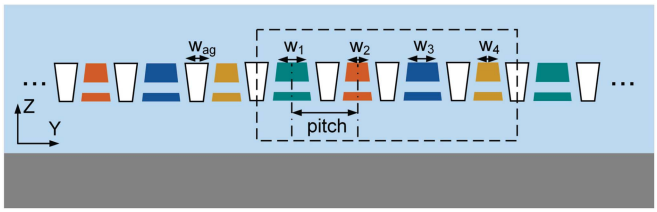

Fig. 6. The structure of the SC_4 AGW superlattices.

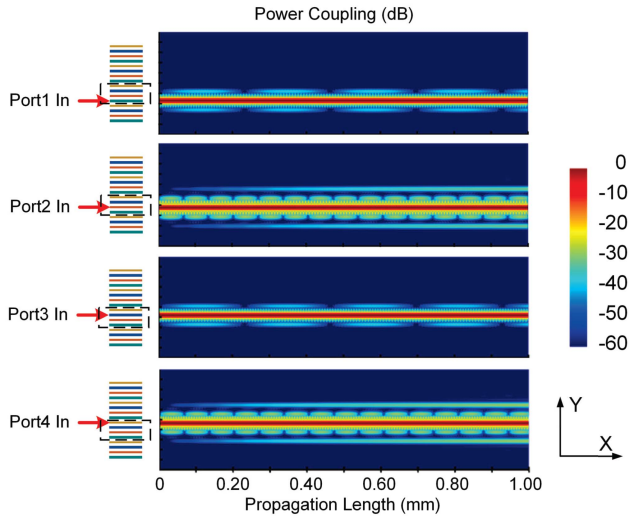

Fig. 7. The profile of the normalized propagation field power in the SC_4 AGW superlattice at 905 nm. The waveguide superlattice contains four supercells, with the input port switching among the four waveguides in one of the supercells. For port n, the waveguide width is w_n. Here, n = 1,2,3,4, $w_1 = 559$ nm, $w_2 = 334$ nm, $w_3 = 546$ nm, and $w_4 = 317$ nm.

crosstalk. Waveguide superlattices [26] represent a practical scheme to solve this problem. In the SC_n waveguide superlattice, the waveguide array consists of repeated supercells, and each supercell contains waveguides with n sets of width. The intrasupercell crosstalk is reduced by the propagation constant difference due to width variation, while the intersupercell crosstalk is also suppressed since the supercell size is n times the adjacent waveguide pitch.

A SC_4 AGW superlattice is designed to achieve low crosstalk in the waveguide array. The structure is shown in Fig. 6, where the waveguide pitch is 0.9 μm, the gap ratio is 50%, the propagation length is $L = 1$ mm, and the other parameters are as listed in Table I.

The design of the SC_4 superlattice should satisfy the following principles. First, the widths of the nearest adjacent waveguides should be appropriately chosen within the range as shown in the red box of Fig. 5(a) to suppress the crosstalk below -20 dB by the effective index difference. So the waveguide widths are alternately wide and narrow in a zigzag distribution. Secondly, the widths of the next nearest adjacent waveguides should also be different to avoid synchronous coupling. Here, the direct crosstalk between the narrow waveguides is the main source of crosstalk, since the field restriction is weaker than that of the wide waveguides, and the indirect coupling resulting from the twice direct coupling of nearest adjacent waveguides is relatively low. Therefore, the waveguide widths of the SC_4 superlattice should be $w_1 > w_3 > w_2 > w_4$, and other distributions are equivalently the same considering the periodicity and symmetry. Finally, the intrasupercell synchronous coupling from waveguides with the same width is unavoidable. The minimum waveguide width in the supercell should be selected carefully to keep the crosstalk low enough within the propagation length.

It is trival to find the best solution directly considering the above principles. Therefore, the waveguide widths of the AGW superlattice are optimized by combining the crosstalk calculation and particle swarm optimization (PSO) algorithm to minimize crosstalk in the waveguide array. For each OPA channel, the overall crosstalk is the superposition of crosstalk from any other waveguide to this waveguide. If the crosstalk occurs mainly between waveguides in the local and adjacent supercells, and is sufficiently low, then the overall crosstalk can be suppressed. Thus, to simplify the calculation, only the crosstalk between any two waveguides is considered here. The crosstalk calculation is packaged as a function $XT_{\max} = f(w_1, w_2, w_3, w_4)$ with the input variables of waveguide widths $w_{1,2,3,4}$ and the output variable of maximum crosstalk $XT_{\max}$. Here, the eigenmode solver of Ansys Lumerical software is used to simulate both intrasupercell and intersupercell crosstalk and obtain the maximum crosstalk between any waveguides. Then, the particle swarm optimization solver of the global optimization toolbox in MATLAB is used to minimize the output variable $XT_{\max}$ by selecting the waveguide widths.

The waveguide width range is 0.50 μm to 0.59 μm for $w_{1,3}$ and 0.29 μm to 0.37 μm for $w_{2,4}$, as marked by the red box in Fig. 5(a). Additionally, the waveguide widths are forced to be $w_1 > w_3 > w_2 > w_4$ to avoid the equivalent multiple solutions considering the convergence of the optimization. The optimized waveguide widths for the SC_4 superlattice are 559 nm, 334 nm, 546 nm and 317 nm, the air-gap width is within the range of 227 nm to 234 nm, and the maximum crosstalk $XT_{\max}$ is -24.3 dB at a wavelength of 905 nm.

The normalized propagation field power in the optimized SC_4 waveguide superlattice is shown in Fig. 7. Here, the waveguide superlattice contains four supercells, and the input port switches

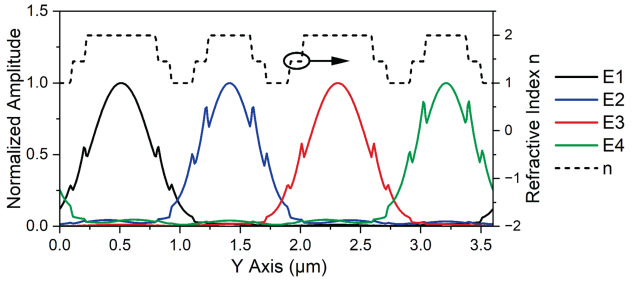

Fig. 8. The profile of the super-mode amplitude and the refractive index of the SC_4 AGW superlattice at 905 nm. In the legend, En corresponds to the super-mode amplitude mainly locates in the waveguide with width w_n. The profiles are at the cutting line of $z = 0.2$ μm.

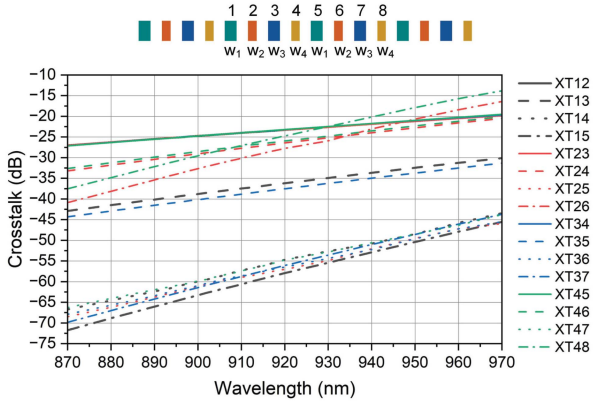

Fig. 9. The crosstalk of the SC_4 AGW superlattice changing with wavelength. The waveguide array contains four groups of supercells, as the inset shows. The crosstalk element $XT_{m,n}$ indicates the crosstalk from input waveguide m to output waveguide n.

among the four waveguides within one of the supercells. For the waveguide of the nth input port, the width is w_n, where $n = 1, 2, 3, 4$. When light is input from the 1st and 3 rd ports, power coupling occurs mainly among the input waveguide, the nearest neighbor waveguide and the second-nearest neighbor waveguide. When light is input from the 2nd and 4th ports, additional power coupling occurs between the waveguides with the same widths, and the power coupling is sufficiently low (< -40 dB) beyond the adjacent supercells. This means that the power coupling is localized within the propagation length below 1 mm, and the crosstalk result is also correct for waveguide arrays with supercell numbers above four.

According to the super-mode profile of the periodic SC_4 superlattice (Fig. 8) calculated by the super-mode approach [36], the waveguide width difference breaks the modes into isolated profiles with low overlap between each other, leading to the low crosstalk.

Furthermore, the wavelength dependence of crosstalk is analyzed by calculating the variation in the main crosstalk elements $XT_{m,n}$ changing with wavelength (Fig. 9), where the crosstalk element $XT_{m,n}$ represents the maximum crosstalk from input waveguide m to output waveguide n over the propagation length. All crosstalk elements are positively related to the wavelength, and the maximum crosstalk elements correspond to the crosstalk between nearest neighbor waveguides, changing from -27.0 dB to -22.5 dB in the wavelength range of 870 nm to 930 nm. And

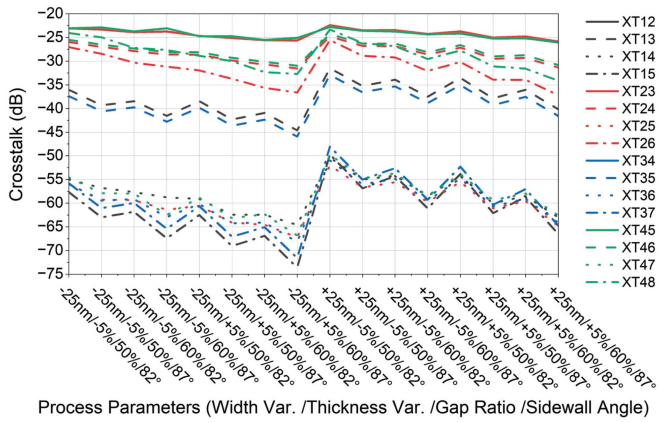

Fig. 10. Worst-case analysis of the SC_4 AGW superlattice crosstalk performance with process variation.

in the wavelength range above 930 nm, the maximum crosstalk elements correspond to the intrasupercell crosstalk $XT_{4,8}$ and $XT_{2,6}$ between the narrower waveguides with the same width, which exceed -20 dB when the wavelength is above 940 nm. For the wavelength range below 870 nm, the maximum crosstalk is lower, but the waveguide supports TE01 mode, which is unexpected. Therefore, the wavelength window satisfying both single-mode condition and crosstalk below -20 dB is from 870 nm to 940 nm. And in the wavelength range from 890 nm to 920 nm, the crosstalk is changing from -25.5 dB to -23.2 dB, showing a slight dependence on the wavelength variation.

III. Process Tolerance Analysis of the AGW Superlattice

The process tolerance of the SC_4 AGW superlattice is also studied by worst-case analysis and Monte-Carlo analysis. The standard parameters and the typical process variations are listed in Table II, including the thickness variations of silicon nitride and silicon oxide in the thin-film deposition process, the width variations in the lithography process, the gap ratio variation in the gap-filling process, and the sidewall angle variation of the waveguide and air gap in the etching process. Here, the statistical probability of each parameter is assumed to obey normal distribution, and the variation corresponds to ± 3 sigma.

The worst-case analysis (Fig. 10) shows that the maximum crosstalk is negatively related to the thickness variation, the gap ratio and the sidewall angle but positively related to the width variation. The maximum crosstalk of the designed AGW superlattice is below -22.4 dB over the process variations at a wavelength of 905 nm.

The worst-case analysis considers only the corner cases of variations that can cover the worst performance of crosstalk if the crosstalk is linearly related to all the process parameters. In contrast, the Monte-Carlo analysis is not based on the linearity assumption and may provide the statistical probability of the crosstalk performance. As the result of Monte-Carlo analysis based on 750 samples shows(Fig. 11), the maximum crosstalk is within the range given by the worst-case analysis between -25.9 dB and -22.4 dB, and more than 91% samples have a

TABLE II
THE PROCESS VARIATIONS OF THE AGW SUPERLATTICE

Parameter Type	t_1	g_1	t_2	$w_{1,2,3,4}$	Gap Ratio	α	β
Standard Value	75 nm	100 nm	275 nm	559 nm, 334 nm, 546 nm, 317nm	50%	86°	86°
Variations	$[-5\%, 5\%]$	$[-5\%, 5\%]$	$[-5\%, 5\%]$	[-25 nm, 25 nm]	[0%, 10%]	$[-4^\circ, 1^\circ]$	$[-4^\circ, 1^\circ]$

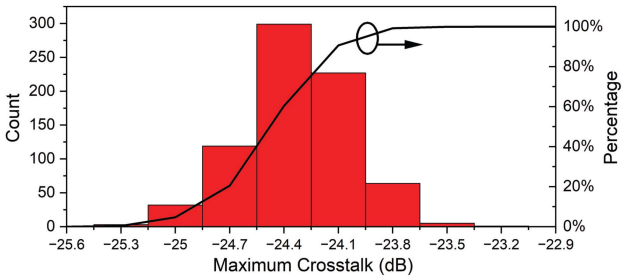

Fig. 11. Monte-Carlo analysis of the SC_4 AGW superlattice crosstalk performance with process variation.

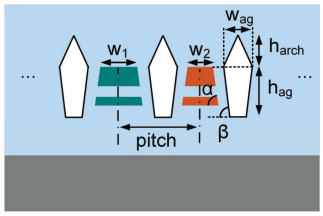

Fig. 12. The AGW structure with a pointed arch air-gap shape.

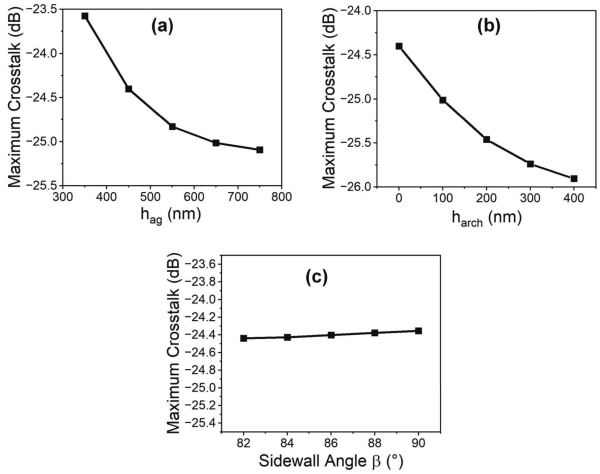

Fig. 13. The maximum crosstalk of a pair of asymmetric AGWs changing with the air-gap height h_{ag} (a), arch height h_{arch} (b), and sidewall angle β (c). In (a), the arch height h_{arch} is 0 nm and the sidewall angle β is 86°; in (b), the air-gap height h_{ag} is 450 nm and the sidewall angle β is 86°; in (c), the air-gap height h_{ag} is 450 nm and the arch height h_{arch} is 0 nm.

maximum crosstalk below -24.1 dB, indicating the robustness with respect to process variations.

IV. DISCUSSION

The air-gap silicon nitride waveguide superlattice is demonstrated to suppress crosstalk below -20 dB at a waveguide pitch of 0.9 μm and a wavelength of 905 nm, which is applicable for OPA with both edge emission [1] and surface emission based on slab diffraction grating [12], [17]. Compared to previous studies [18], [19], this work steps forward to reduce the waveguide pitch and increase the beam steering angle of the OPA.

Notably, the shape and size of the air gaps are highly dependent on the preparation process. Formed by the nonconformal chemical vapor deposition method [35], the air gaps are typically in the shape of a pointed arch, as depicted in Fig. 12, which can be defined by the air-gap height h_{ag}, the arch height h_{arch}, the air-gap width w_{ag}, and the sidewall angle β.

The influence of the air-gap shape on the maximum crosstalk of a pair of asymmetric AGWs is also analyzed (Fig. 13), where the waveguide widths are $w_1 = 559$ nm and $w_2 = 334$ nm, the pitch is 0.9 μm, the propagation length is 1 mm, the gap ratio is 50%, the wavelength is 905 nm, and the layer thicknesses and sidewall angle of the waveguide are the same as in Table I. The maximum crosstalk is negatively related to the air-gap height, decreasing from -23.6 dB to -25.1 dB in accordance with the air-gap height varying from 350 nm to 750 nm, where the arch height is 0 nm, and the sidewall angle is 86° (Fig. 13(a)). The maximum crosstalk is also negatively related to the arch height, decreasing from -24.4 dB to -25.9 dB in accordance with the arch height increasing from 0 nm to 400 nm, where the air-gap height is 450 nm, and the sidewall angle is 86° (Fig. 13(b)). The maximum crosstalk is almost independent of the sidewall angle, where the center width of the air gap is constant, i.e., $w_{ag} = (pitch - w_1/2 - w_2/2)/2 - h_{ag}\cot(86^\circ) + h_{ag}\cot\beta$, the air gap height is 450 nm, and the arch height is 0 nm (Fig. 13(c)). Therefore, the simplified shape in Fig. 1 is sufficiently accurate since the maximum crosstalk of the waveguide array varies slightly when the air-gap shape changes within the range considered in Fig. 13.

In addition, on OPA or solid-state LiDAR chips, there are typically waveguides and components such as edge or grating couplers, beam splitters, phase shifters, and diffraction gratings in the layout. Introducing air gaps in most of these components may result in performance deterioration. Therefore, the preparation process needs to be carefully designed to locate the air gaps in a particular area. One of the possible preparation methods is separating the patterns with and without air gaps into two steps. In the first step, the waveguide and components are prepared by lithography and etching, with all gaps well filled with the cladding material. In the second step, the waveguide array with air gaps is prepared, with air gaps formed by poor filling. Adiabatic tapers with high alignment tolerance [37] may be used to connect the waveguides between the two patterns. An alternative preparation method is to use hybrid lithography technology, forming all components with and without air gaps by ultraviolet lithography and etching, and then selectively filling the gaps by using electron beam lithography (EBL) based on hydrogen silsesquioxane (HSQ) photoresist [38].

V. Conclusion

We have achieved improved crosstalk suppression using the proposed multilayer silicon nitride AGW superlattices. First, the AGW is demonstrated to have a smaller skin depth of the evanescent field and a higher single-mode effective index than the NAGW, according to the mode analysis. Next, lower power crosstalk is demonstrated between a pair of AGWs than the NAGWs by the crosstalk calculation using the eigenmode expansion method. Finally, a SC_4 AGW superlattice is designed and analyzed theoretically. The maximum crosstalk of the waveguide array is suppressed to -24.3 dB at a waveguide pitch of 0.9 μm, propagation length of 1 mm, and wavelength of 905 nm. The propagation field simulation shows that the power coupling is localized within the input and adjacent supercells, indicating no degradation with scale-up of the waveguide array.

The crosstalk of the SC_4 AGW superlattice shows slight wavelength dependence, remaining below -23.2 dB over the wavelength range of 890 nm to 920 nm. According to the worst-case analysis, the crosstalk is still below -22.4 dB under the lithography pattern width variation of ± 25 nm, the waveguide layer thickness variation of $\pm 5\%$, the gap ratio from 50% to 60%, and the sidewall angle from 82° to 87°, showing good process tolerance.

Therefore, the proposed AGW superlattice reduces the spacing of the silicon nitride waveguide array, showing potential to improve the beam steering performance of the OPA chips with respect to the near-infrared (NIR) waveband.

Acknowledgment

The authors are grateful to Xinqun Zhang, Liang Zhou for helpful discussion on the preparation process.

References

[1] D. Kwong, A. Hosseini, Y. Zhang, and R. T. Chen, "1×12 unequally spaced waveguide array for actively tuned optical phased array on a silicon nanomembrane," *Appl. Phys. Lett.*, vol. 99, no. 5, 2011, Art. no. 051104.

[2] D. Kwong et al., "Corrugated waveguide-based optical phased array with crosstalk suppression," *IEEE Photon. Technol. Lett.*, vol. 26, no. 10, pp. 991–994, May 2014.

[3] D. Kwong et al., "On-chip silicon optical phased array for two-dimensional beam steering," *Opt. Lett.*, vol. 39, no. 4, pp. 941–944, 2014.

[4] D. N. Hutchison et al., "High-resolution aliasing-free optical beam steering," *Optica*, vol. 3, no. 8, pp. 887–890, 2016.

[5] C. V. Poulton et al., "Coherent solid-state LIDAR with silicon photonic optical phased arrays," *Opt. Lett.*, vol. 42, no. 20, pp. 4091–4094, 2017.

[6] T. Komljenovic, R. Helkey, L. Coldren, and J. E. Bowers, "Sparse aperiodic arrays for optical beam forming and LIDAR," *Opt. Exp.*, vol. 25, no. 3, pp. 2511–2528, 2017.

[7] C. V. Poulton et al., "Long-range LiDAR and free-space data communication with high-performance optical phased arrays," *IEEE J. Sel. Topics Quantum Electron.*, vol. 25, no. 5, pp. 1–8, Sep./Oct. 2019.

[8] Y. Zhang et al., "Sub-wavelength-pitch silicon-photonic optical phased array for large field-of-regard coherent optical beam steering," *Opt. Exp.*, vol. 27, no. 3, pp. 1929–1940, 2019.

[9] W. Xu, L. Zhou, L. Lu, and J. Chen, "Aliasing-free optical phased array beam-steering with a plateau envelope," *Opt. Exp.*, vol. 27, no. 3, pp. 3354–3368, 2019.

[10] C.-S. Im, B. Bhandari, K.-P. Lee, S.-M. Kim, M.-C. Oh, and S.-S. Lee, "Silicon nitride optical phased array based on a grating antenna enabling wavelength-tuned beam steering," *Opt. Exp.*, vol. 28, no. 3, pp. 3270–3279, 2020.

[11] S. A. Miller et al., "Large-scale optical phased array using a low-power multi-pass silicon photonic platform," *Optica*, vol. 7, no. 1, pp. 3–6, 2020.

[12] P. Wang et al., "Design and fabrication of a SiN-Si dual-layer optical phased array chip," *Photon. Res.*, vol. 8, no. 6, pp. 912–919, 2020.

[13] C.-P. Hsu et al., "A review and perspective on optical phased array for automotive LiDAR," *IEEE J. Sel. Topics Quantum Electron.*, vol. 27, no. 1, Jan./Feb. 2021, Art no. 8300416.

[14] G. Luo et al., "Demonstration of 128-channel optical phased array with large scanning range," *IEEE Photon. J.*, vol. 13, no. 3, pp. 1–10, Jun. 2021.

[15] Y. Li et al., "Wide-steering-angle high-resolution optical phased array," *Photon. Res.*, vol. 9, no. 12, pp. 2511–2518, 2021.

[16] C. V. Poulton et al., "Coherent LiDAR with an 8,192-element optical phased array and driving laser," *IEEE J. Sel. Topics Quantum Electron.*, vol. 28, no. 5, Sep./Oct. 2022, Art. no. 6100508.

[17] Y. Liu and H. Hu, "Silicon optical phased array with a 180-degree field of view for 2D optical beam steering," *Optica*, vol. 9, no. 8, pp. 903–907, 2022.

[18] N. A. Tyler et al., "SiN integrated optical phased arrays for two-dimensional beam steering at a single near-infrared wavelength," *Opt. Exp.*, vol. 27, no. 4, pp. 5851–5858, 2019.

[19] S. Monfray et al., "Optical phased array for 905-nm LIDAR applications integrated on 300 mm Si-photonic platform," in *Proc. IEEE Opt. Fiber Commun. Conf. Exhib.*, 2022, pp. 1–3.

[20] B. E. A. Saleh and M. C. Teich, *Fundamentals of Photonics*. Hoboken, NJ, USA: Wiley, 1991.

[21] K. Li et al., "Crosstalk analysis of silicon-on-insulator nanowire-arrayed waveguide grating*," *Chin. Phys. B*, vol. 25, 2016, Art. no. 124209.

[22] G. Zhou, S.-W. Qu, J. Wu, and S. Yang, "Design of a low-crosstalk sub-wavelength-pitch silicon waveguide array for optical phased array," *IEEE Photon. J.*, vol. 13, no. 4, Aug. 2021, Art. no. 2200608.

[23] S. Jahani et al., "Controlling evanescent waves using silicon photonic all-dielectric metamaterials for dense integration," *Nature Commun.*, vol. 9, 2018, Art. no. 1893.

[24] A. Khavasi, L. Chrostowski, Z. Lu, and R. Bojko, "Significant crosstalk reduction using all-dielectric CMOS-compatible metamaterials," *IEEE Photon. Technol. Lett.*, vol. 28, no. 24, pp. 2787–2790, Dec. 2016.

[25] M. B. Mia, S. Z. Ahmed, I. Ahmed, Y. J. Lee, M. Qi, and S. Kim, "Exceptional coupling in photonic anisotropic metamaterials for extremely low waveguide crosstalk," *Optica*, vol. 7, no. 8, pp. 881–887, 2020.

[26] W. Song et al., "High-density waveguide superlattices with low crosstalk," *Nature Commun.*, vol. 6, no. 1, 2015, Art. no. 7027.

[27] N. Yang et al., "Theory of high-density low-cross-talk waveguide superlattices," *Photon. Res.*, vol. 4, no. 6, pp. 233–239, 2016.

[28] L.-M. Leng, Y. Shao, P.-Y. Zhao, G.-F. Tao, S.-N. Zhu, and W. Jiang, "Waveguide superlattice-based optical phased array," *Phys. Rev. Appl.*, vol. 15, Jan. 2021, Art. no. 14019.

[29] S. Longhi et al., "Observation of dynamic localization in periodically curved waveguide arrays," *Phys. Rev. Lett.*, vol. 96, Jun. 2006, Art. no. 243901.

[30] N. Grossard, J. Hauden, and H. Porte, "Periodic anticoupling structures for parallel optical waveguides on $LiNbo_3$," *J. Lightw. Technol.*, vol. 29, no. 16, pp. 2489–2495, Aug. 2011.

[31] X. Yi, H. Zeng, S. Gao, and C. Qiu, "Design of an ultra-compact low-crosstalk sinusoidal silicon waveguide array for optical phased array," *Opt. Exp.*, vol. 28, no. 25, pp. 37505–37513, 2020.

[32] L. Wang et al., "Design of a low-crosstalk half-wavelength pitch nano-structured silicon waveguide array," *Opt. Lett.*, vol. 44, no. 13, pp. 3266–3269, 2019.

[33] C. G. H. Roeloffzen et al., "Low-loss Si3N4 TriPleX optical waveguides: Technology and applications overview," *IEEE J. Sel. Topics Quantum Electron.*, vol. 24, no. 4, Aug. 2018, Art. no. 4400321.

[34] Q. Han, M. Ménard, and W. Shi, "Superlattice arrayed waveguide grating in silicon nitride," *IEEE Photon. Technol. Lett.*, vol. 32, no. 22, pp. 1411–1414, Nov. 2020.

[35] B. Shieh et al., "Air-gap formation during IMD deposition to lower interconnect capacitance," *IEEE Electron Device Lett.*, vol. 19, no. 1, pp. 16–18, Jan. 1998.

[36] I. Cerutti, N. Andriolli, and P. Velha, "Engineering of closely packed silicon-on-isolator waveguide arrays for mode division multiplexing applications," *J. Opt. Soc. Am B*, vol. 34, no. 2, pp. 497–506, 2017. [Online]. Available: https://opg.optica.org/josab/abstract.cfm?URI=josab-34-2-497

[37] N. Ye et al., "High-alignment-accuracy transfer printing of passive silicon waveguide structures," *Opt. Exp.*, vol. 26, no. 2, pp. 2023–2032, 2018.

[38] L. Mollard, G. Cunge, S. Tedesco, B. Dal'zotto, and J. Foucher, "HSQ hybrid lithography for 20 nm CMOS devices development," *Microelectronic Eng.*, vol. 61/62, pp. 755–761, 2001.